

Supplementary Information for

Gate-voltage-induced reversible electrical phase transitions in $\text{Mo}_{0.67}\text{W}_{0.33}\text{Se}_2$ devices

Min-Sik Kim^{1,2†}, Dong-Hwan Choi^{1,2†}, In-Ho Lee², Wu-Sin Kim¹, Duhyuk Kwon^{2,3}, Myung-Ho Bae^{2,4*}, Ju-Jin Kim^{1*}

¹Department of Physics, Jeonbuk National University, Jeonju 54896, Republic of Korea

²Korea Research Institute of Standards and Science, Daejeon 34113, Republic of Korea

³Department of physics, Chungnam National University, Daejeon 34134, Republic of Korea

⁴Department of Nano Science, University of Science and Technology, Daejeon, 34113, Republic of Korea

†These authors contributed equally to this work.

*e-mail: mhbae@kriss.re.kr; jujinkim@chonbuk.ac.kr

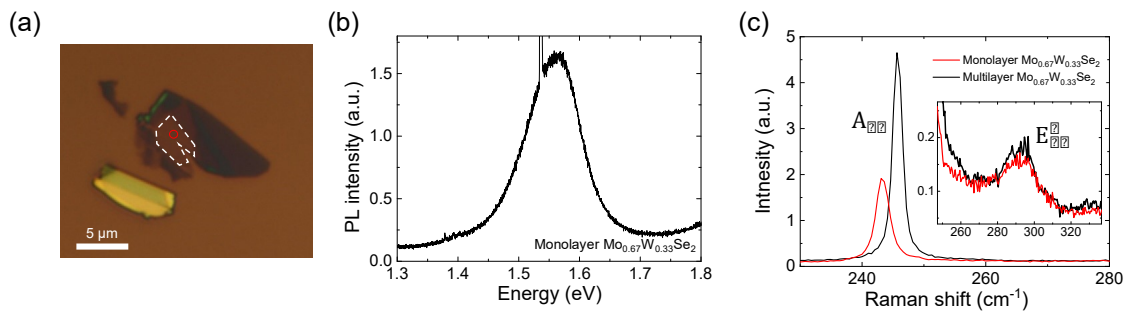
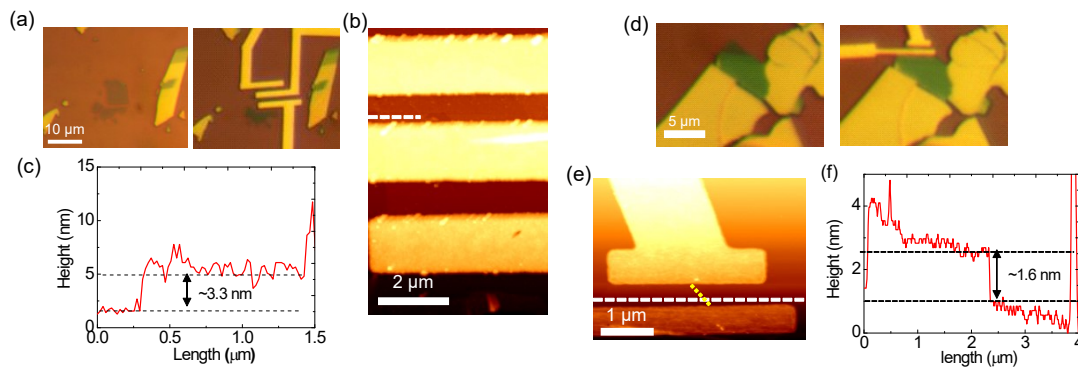


Figure S1. (a) Optical image of another monolayer MoWSe flakes (a region outlined by a dashed line). The Photoluminescence (PL) and Raman spectra were taken at the red-circle region. (b) PL spectrum of the monolayer flake, which shows a peak at 1.56 eV. (c) Raman spectrum of monolayer (red curve) and multilayer (black one) flakes. A_{1g} peak observed at 243.23 cm^{-1} for the monolayer is shifted to 245.73 cm^{-1} for the multilayer. The inset shows



E_{2g}^1 peaks over $287.30 - 297.43 \text{ cm}^{-1}$. These observations are consistent with a previous report.¹

Figure S2. (a) Optical microscope images after exfoliation (left panel) and deposition electrodes (right one) for trilayer device. (b) Atomic force microscope (AFM) image of the $n = 4$ device. (c) Height profile along a dashed line in (b). (d) Optical microscope images after exfoliation (left panel) and deposition electrodes (right one) for monolayer device. (e) Atomic force microscope (AFM) image of the trilayer device. Dotted yellow line indicates a boundary of the monolayer MoWSe. (f) Height profile along a dashed line in (e). The layer number was

estimated by considering the thickness of a monolayer deposited on SiO_2 (~ 1.6 nm) and thickness of one layer (0.65 nm).

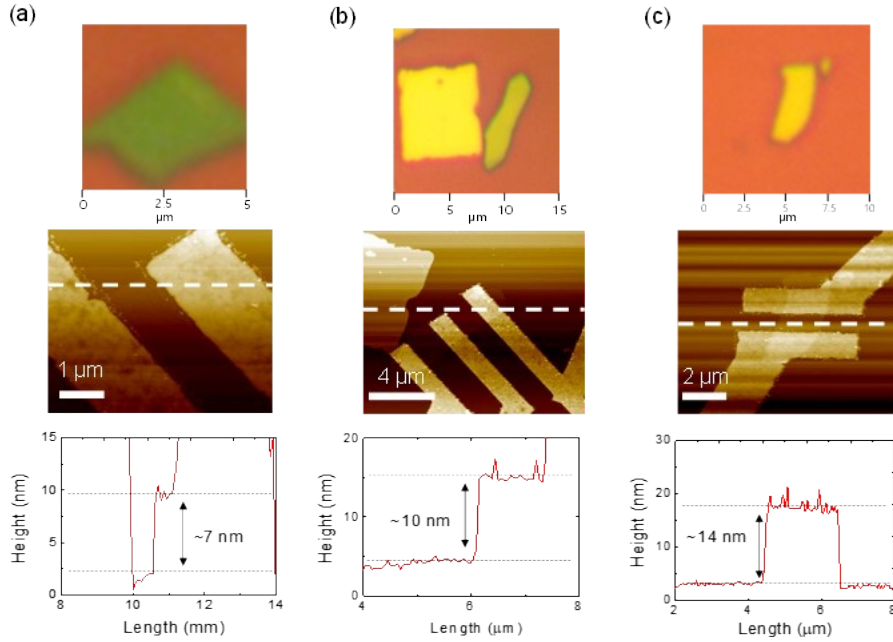
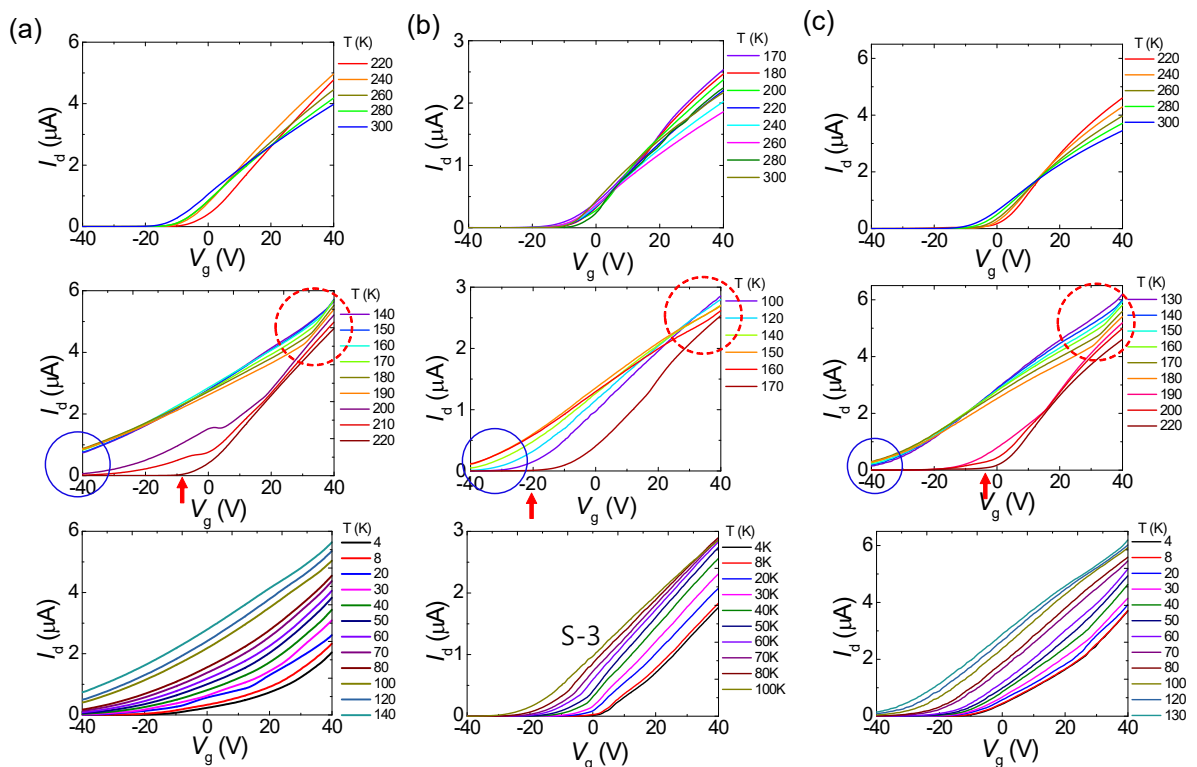
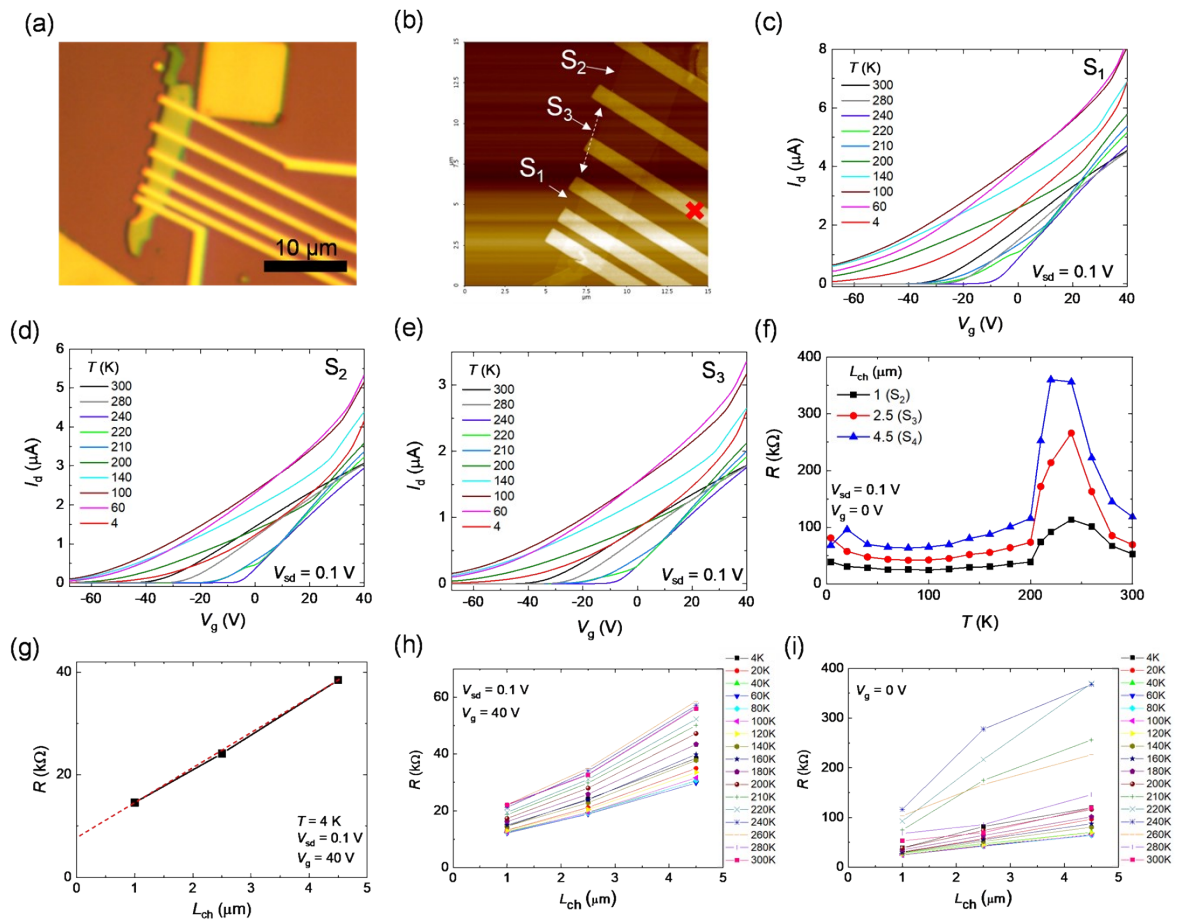


Figure S3. (a)-(c) Top panels: optical microscope images of exfoliated MoWSe flakes, middle panels: AFM images of MoWSe devices with 100 nm thick In electrodes. Bottom panels:



height profiles of 7, 10 and 14 nm thick devices, respectively.

Figure S4. (a)-(c) Transfer curves for three temperature groups of 7, 10 and 14 nm thick devices, respectively ($V_{sd} = 0.1$ V). Middle panels show deflection behavior in transfer curves in dashed circles. The red arrows indicate the threshold voltage (V_{th}) of the n_o branches for the devices. The V_{th} locations for the n' branches, as depicted by blue-circled regions, are



distinguished from the V_{th} locations of the n_o branches for all devices.

Figure S5. (a),(b) Optical microscope and AFM images of a ~ 10 nm thick MoWSe device ($n \sim 13$) with multiple In electrodes, respectively. We performed the transfer length method (TLM) with the multiple electrodes with different intervals to get a contact resistance (R_c). The

device dimension information is shown in Supplementary Table S1. In (b), devices denoted by S_m ($m = 1, 2$ and 3) were used for the TLM. The electrode indicated by the red cross showed a bad contact property, thus we used the channel, S_3 , across the bad electrode. (c)-(e) Transfer curves for various temperatures of the three devices. (f) Resistance (R) as a function of T for the three devices at $V_g = 0$ V, which shows an abrupt change in R at $T \sim 200$ K. (g) R as a function of a channel length (L_{ch}) at $V_g = 40$ V and $T = 4$ K, which was obtained from (c)-(e). By the linear extrapolation from the three data points, we get a resistance at $L_{ch} = 0$ μm , which corresponds to $2R_c$. (h),(i) R - L_{ch} curves for various temperatures at $V_g = 40$ and 0 V, which provide R_c as a function of T , as shown in Fig. 2e in the main panel.

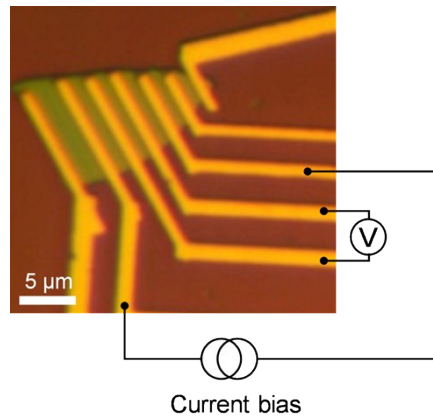


Figure S6. Optical microscope image of the MoWSe device ($n \sim 10$, $L_{ch} = 1$ μm for the channel to be measured) with a four-probe experimental configuration.

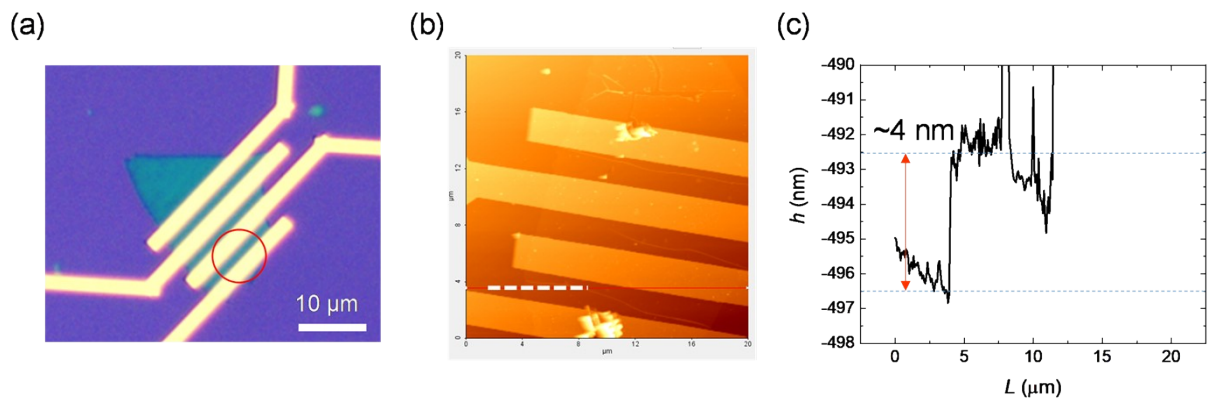


Figure S7. (a) Optical microscope image of $n = 5$ MoWSe device with Ti/Au contact electrodes. Scale bar: $10 \mu\text{m}$. The channel indicated by the red circle was used in the measurement. (b),(c) AFM image of the device and the height profile along the dashed line in (b), respectively.

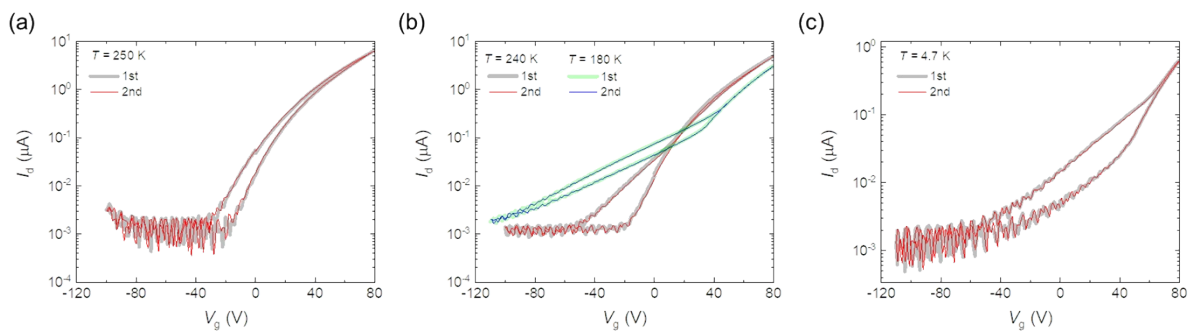


Figure S8. Repetitive scanning of representative transfer curves in Figure 3a-c in the main panel.

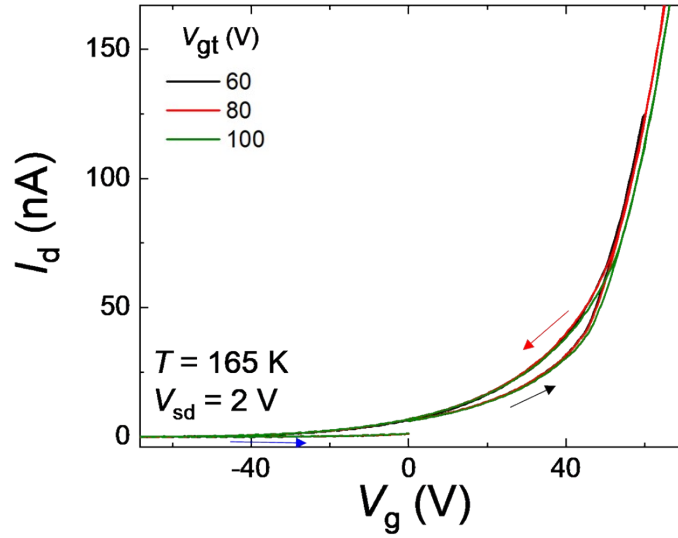


Figure S9. Transfer curves for various V_{gt} values for the $n = 5$ MoWSe device, where the gate sweep was started along a black curve from $V_g = 0$ V, followed by red and blue arrows.

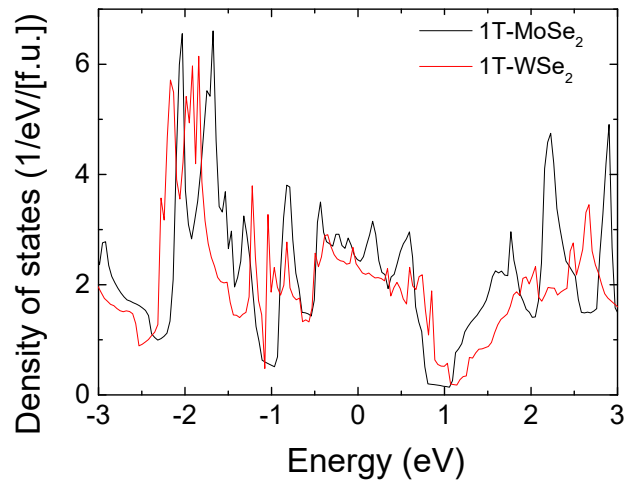


Figure 10. Density of states of 1T-MoSe₂ and 1T-WSe₂, which show metallic phases at the Fermi level ($E = 0$ eV). First principle DFT calculations² were performed using the generalized gradient approximation³ for the exchange-correlation potential and the projector-augmented wave potentials,⁴ as implemented in the VASP code.⁵ The wave functions were expanded in

plane waves to an energy cutoff of 500 eV. We used a supercell geometry with a vacuum region larger than 20 Å to prevent interactions between adjacent supercells. For given ionic positions, the enthalpy of the system was minimized at zero pressure by performing density functional calculations. Using a \mathbf{k} -point mesh with a grid spacing of $2\pi \times 0.03 \text{ \AA}^{-1}$, we repeated the iterative procedure until all the forces and stress tensors were less than 0.01 eV/Å and 1.5 kbar, respectively. For density-of-states calculations, Kohn–Sham eigenvalues,⁶ including spin–orbit coupling, were calculated on a high-resolution \mathbf{k} -point mesh with a grid spacing of $2\pi \times 0.01 \text{ \AA}^{-1}$, corresponding to ~ 1300 \mathbf{k} points in the irreducible Brillouin zone.

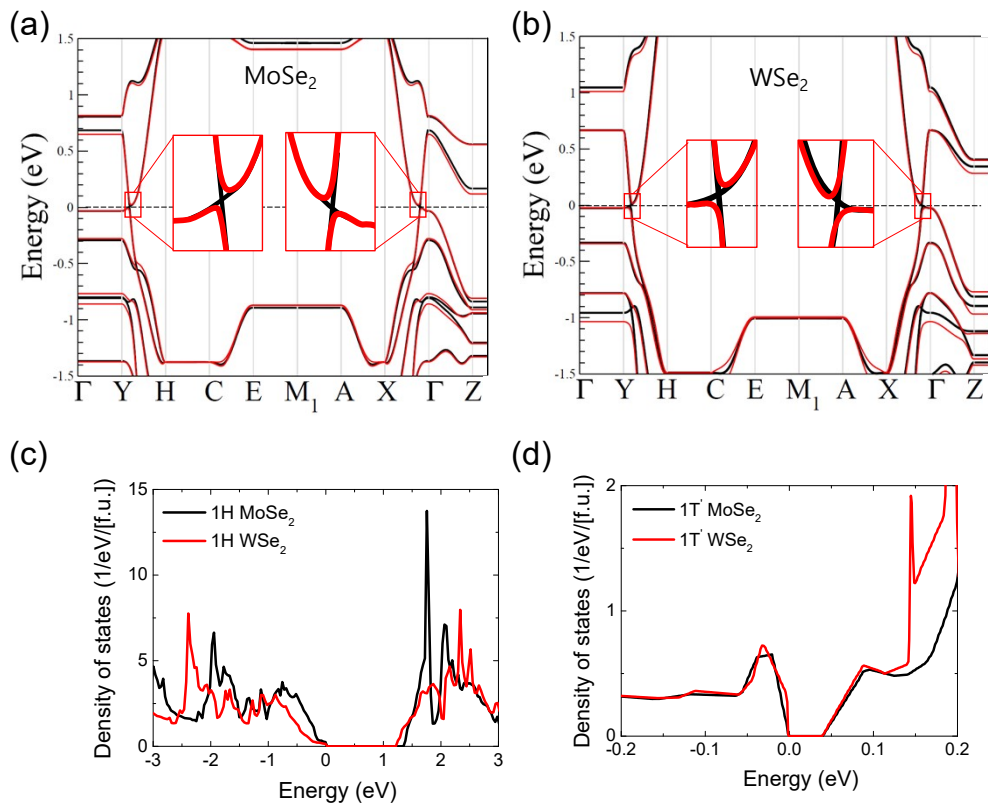


Figure S11. (a), (b) Electronic bands without (black) and with (red) spin-orbit coupling of 1T' phases for MoSe₂ and WSe₂, respectively. Insets: Schematic plots of the boxed regions in the main panels. (c),(d) Density of states for 1H and 1T' phases, respectively, of MoSe₂ and WSe₂.

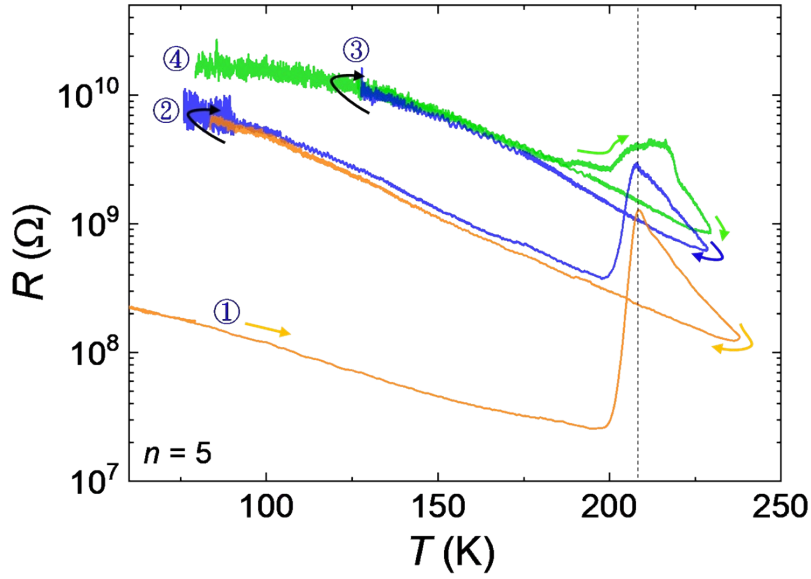


Figure S12. Resistance (R) as a function of T for multiple temperature sweeps assigned by numbers and arrows ($V_{sd} = 3$ V and $V_g = 40$ V) of the $n = 5$ MoWSe device.

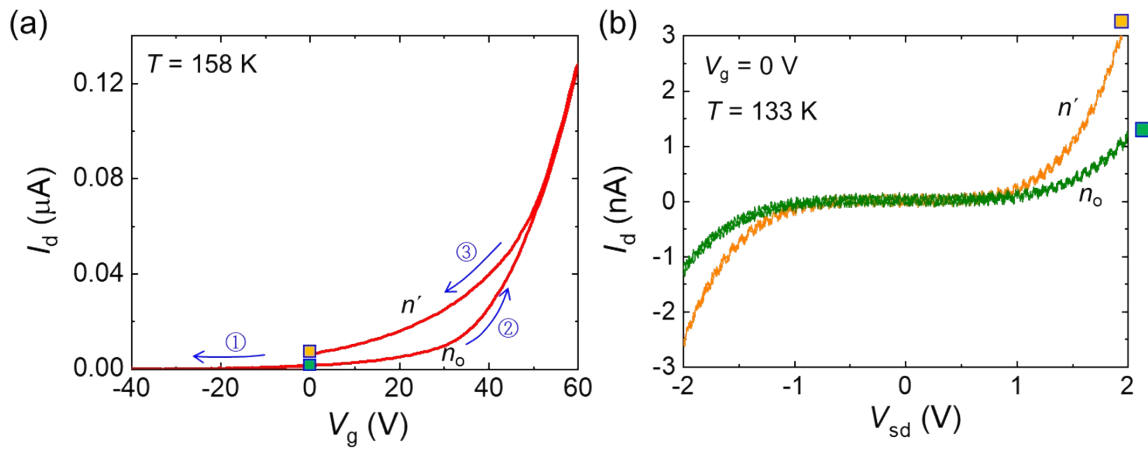


Figure S13. Hysteretic transfer curve at $T = 158$ K at $V_{sd} = 2$ V for the $n = 5$ device shown in Fig. 3. Arrows and assigned numbers indicates the sweep direction and sweep order, respectively. When we swept V_g from 0 (indicated by the green box) to -40 V (sweep ①) followed by the forward sweep ② to $V_g = 60$ V, it did not form a hysteresis in the n_o state. Finally, it showed the n_o -to- n' transition by the sweep ③. (b) I_d - V_{sd} curves obtained at n' and

n_o states at $V_g = 0$ V in (a) at $T = 133$ K. It shows two I_d - V_{sd} curves obtained at $V_g = 0$ V in the n' (orange curve) and n_o (green one) states, which show ~ 3 and ~ 1 nA at $V_{sd} = 2$ V, respectively. This indicates that each state was kept for a range of $|V_{sd}| < 2$ V without a phase transition. Thus, we believe that there was no formation of metal filament between source and drain electrodes.⁷ Another possibility is the formation of the metal filament between the drain electrode and highly doped Si substrate through 500 nm thick SiO₂ layer. However, the case cannot explain the different curvatures in I_d - V_{sd} curves for the n' and n_o states shown in (b) because the current along the metal filament through the SiO₂ should just play as an offset current for the source-drain I_d - V_{sd} characteristics.

Device number	Thickness (nm)	W_{ch} (μm)	L_{ch} (μm)
S ₁	10	3.0	1.0
S ₂	13	4.0	2.5
S ₃	10	3.6	4.5

Table S1. Geometrical dimensions of used devices for the TLM.

Table S2. Conductance values of four-layer and monolayer devices at given V_g values and its ratio.

V_g (V)	G (μS) for $n = 4$	G for $n = 1$	$G_{n=4}/G_{n=1}$
-20	2.84	1.17	2.42
-30	2.04	0.625	3.26
-40	1.41	0.285	4.94
-50	0.93	0.11	8.45
-60	0.7	0.05	14

References for supplementary information

1. M., Zhang, *et al. ACS Nano*, 2014, **8**, 7130-7137.
2. P. Hohenberg and W. Kohn, *Phys. Rev.*, 1964, **136**, B864-71.
3. J. P. Perdew, K. Burke and M. Ernzerhof, *Phys. Rev. Lett.*, 1996, **77**, 3865-8.
4. G. Kresse and D. Joubert, *Phys. Rev. B*, 1999, **59**, 1758-75.
5. G. Kresse, and J. Furthmüller, *Comp. Mater. Sci.*, 1996, **6**, 15-50.
6. W. Kohn and L. J. Sham, *Phys. Rev.*, 1965, **140**, A1133-8.
7. H. Tian, X. Wang, H. Zhao, W. Mi, Y. Yang, P.-W. Chiu, and T.-L. Ren, *Adv. Electron. Mater.* 2018, **2018**, 1700608.